PHYSICAL REVIEW A **97**, 063836 (2018)

Nonlinear coupled-mode-theory framework for graphene-induced saturable absorption in nanophotonic resonant structures

Vasileios G. Ataloglou, Thomas Christopoulos,[*] and Emmanouil E. Kriezis
Department of Electrical and Computer Engineering, Aristotle University of Thessaloniki (AUTH), Thessaloniki 54124, Greece

(Received 23 February 2018; published 21 June 2018)

A strict mathematical framework combining perturbation theory and temporal coupled-mode theory is developed to model graphene-induced saturable absorption in graphene-enhanced nanophotonic resonators. To allow for loss saturation in graphene, a power-dependent model of its surface conductivity is carefully introduced, based on the underlying physics. The framework is then cautiously unfolded to capture the two-dimensional nature of graphene and its interaction with the electromagnetic mode, additionally allowing one to incorporate any bulk or sheet material that is subject to saturable loss, together with other nonlinear effects. Both exact and approximative approaches are introduced, revealing the capabilities of the proposed framework to address the effect of saturable absorption. A graphene-enhanced silicon slab ring resonator is examined using the developed framework, uncovering its excellent accuracy and its capability to downgrade the computational complexity of a full-wave nonlinear simulation to a phenomenological but physically definitive differential equation. The potential of the resonant structure to act as an optically addressed switching element is being demonstrated, exposing high extinction ratio and low power requirements. Finally, it is illustrated how the framework is capable of capturing the rich dynamics of a resonant system that may additionally exhibit Kerr- and/or free-carrier-induced optical bistability and self-pulsation.

DOI: 10.1103/PhysRevA.97.063836

I. INTRODUCTION

Graphene has attracted substantial interest in the past decade due to its unique thermal, mechanical, electrical, and optical properties [1]. Especially for photonic applications, graphene features a vast mixture of appealing characteristics such as broadband spectral response, extensive tunability, relatively low resistive losses, and high nonlinear response [2]. The graphene growth using chemical vapor deposition (CVD) combined with the mature photonic integration technology led to the development of numerous electrically controlled, guided-wave applications in the near-infrared (NIR) optical regime [3–6], while the possibility for practical plasmonic devices based on graphene has also been explored [7].

Almost concurrently several groups have started to explore nonlinear properties associated with graphene. Early theoretical works indicated that graphene exhibits a strong third-order nonlinear response (Kerr effect) [8] and non-negligible nonlinear losses owing to the two-photon absorption process [9]. As a consequence, a multitude of functional nonlinear devices have been proposed and computationally analyzed [10–13], all treating graphene nonlinearities as a small perturbation of its linear properties. Recently, it has experimentally been verified through independent measurements that graphene indeed exhibits a strong nonlinearity of Kerr type [14–16], upholding earlier experiments on four-wave mixing with graphene-enhanced photonic resonators [17,18].

Apart from the aforementioned nonlinearities, the intensity dependent quench of linear losses [i.e., saturable absorption (SA)] has so far given the most promising functional devices that have been theoretically studied and experimentally demonstrated. SA in graphene has a low saturation intensity and a broadband response, spanning from millimeter waves [19] to the NIR [20], owing to the inherently different nature of interband and intraband absorption processes. Based on these ascertainments, early works on graphene SA demonstrated practical applications that ranged from fiber-based mode-locked [21–23] and Q-switched [24,25] pulsed lasers to solid-state lasers [26], pulse shaping [27], and vertical-external-cavity surface-emitting lasers [28]. Recently, SA has experimentally been observed in graphene-enhanced silicon integrated waveguides of wire and slot type [29–31], showing a remarkable modulation depth due to the deep light confinement and the relatively long interaction length that silicon-on-insulator (SOI) technology provides.

In an attempt to further exploit the SA modulation depth and reduce the required operational power, in this work we incorporate graphene with a silicon traveling-wave resonator, in order to capitalize on the intensity build-up of the electromagnetic field that the latter provides. Based on the combination of the first-order perturbation theory and the temporal coupled-mode theory (CMT) [32], we meticulously build an effective nonlinear framework that downgrades the complex spatiotemporal Maxwell's equations into simpler and easier to solve, solely time-dependent differential equations, retaining excellent accuracy, validated here through rigorous full-wave nonlinear simulations. The framework is cautiously developed to allow the incorporation of arbitrary bulk and sheet-type materials, expanding an earlier work that mainly focused on bulk semiconductors [33]. Especially for graphene, the complicated nature of its linear loss saturation is captured

---

[*] cthomasa@ece.auth.gr

to its full extent through the adopted power-dependent model of its surface conductivity, revealing the physical insight of the phenomenon when it is established inside resonant structures. Additionally, the framework is capable of providing design guidelines for high-performance, low-power all-optical switching.

Though our primary focus is on SA, graphene additionally exhibits a strong Kerr effect that may influence the behavior of the resonant system and thus must be taken into account for a more complete picture. This is easily achieved using the proposed CMT-based framework through the incorporation of an additional term, quantifying its relative strength with respect to SA. Conveniently, this term is capable of modeling the Kerr effect not only in graphene, but also in any underlying bulk or sheet nonlinear material [13]. Likewise, other nonlinear electromagnetic phenomena, such as two-photon absorption (TPA) and the emerging free-carrier effects (FCEs) in silicon, can also be incorporated [34] in order to model the resonant system in its full extent. Nevertheless, for the resonant system considered in this work, SA outperforms the Kerr effect, TPA, and FCEs. In all cases, regardless of their relatively weak strength compared to SA, the assortment of the existing nonlinear effects results in rich dynamics for the resonant system that can be explored using the proposed framework when combined with a linear stability analysis [35]. All of the framework capabilities, together with all-optical switching actions, are demonstrated using a simple, yet representative resonant system consisting of a graphene-enhanced silicon slab ring resonator.

The paper is organized as follows. In Sec. II we introduce saturable absorption in graphene and incorporate it into CMT (using first-order perturbation theory) and employ both a strict and an approximative approach which simplifies the analysis. Extra care is taken for the framework to allow the handling of different SA models, allowing one to incorporate a broad range of materials. Following, a two-dimensional graphene-enhanced resonant system is studied in Sec. III, targeting the validation of the developed framework, as well as the demonstration of a SA-based all-optical switching element. Based on the plentiful nonlinear effects appearing in the resonant structure under consideration, in Sec. IV the rich system dynamics are explored. Finally, our work concludes in Sec. V.

II. THEORETICAL FRAMEWORK

In this section, we introduce the saturation of resistive losses in graphene through its linear surface conductivity. Subsequently, we develop a formulation combining perturbation theory and coupled-mode theory to analyze graphene-comprising resonant systems that exhibit saturable absorption.

A. Saturable absorption in graphene

In the context of Maxwell's equations, graphene is modeled by a linear surface conductivity tensor $\bar{\sigma}_s^{(1)}$ to reflect its 2D nature [36]. In the absence of static magnetic field (case studied herein), the tensorial nature of graphene linear conductivity may be reduced to a single parameter σ_1. In that case, the induced surface current density is calculated as $\mathbf{J}_s = \sigma_1 \mathbf{E}_\parallel$, where $\mathbf{E}_\parallel$ are the tangential to the graphene sheet electric-field components. The conductivity parameter σ_1 is the outcome of two types of electron transitions due to single-photon absorption in graphene, namely the interband and intraband absorption. In turn, it is described by the widely known Kubo formula [37].

Despite the unique nature of the graphene energy diagram (which is conoidal shaped near the Dirac point), the absorption process might saturate under relatively intense electric field [20,21], a phenomenon appearing in semiconductors as well, referred to as saturable absorption. Being two remarkably different processes, intraband and interband absorption saturate under different power levels, depending, among others, on the Fermi level μ_c of graphene. Near the $\mu_c = 0$ region (pristine graphene), interband absorption dominates over the intraband process and also saturates at much lower optical intensities [20]. Under these conditions, intraband absorption is regarded as a nonsaturable term for a broad range of input intensities. The dynamic response of SA is often compacted within a single relaxation time $\tau_{\text{relax}} \approx 400$ fs [27]. Consequently, for applications evolving at a rate of a few tens of picoseconds or slower (equivalently for rates around tens of Gbps), we can model SA in graphene as an instantaneous process. In terms of conductivity, graphene losses are related to the real part of the scalar surface conductivity, while the imaginary part refers to the equivalent dielectric properties of graphene. Based on this remark, we model SA in graphene according to

$$\sigma_1 = \sigma_{\text{intra,Re}} + \frac{\sigma_{\text{inter,Re}}}{1 + I/I_{\text{sat}}} + i(\sigma_{\text{intra,Im}} + \sigma_{\text{inter,Im}}), \tag{1}$$

where $\sigma_{\text{intra}} = \sigma_{\text{intra,Re}} + i\sigma_{\text{intra,Im}}$ and $\sigma_{\text{inter}} = \sigma_{\text{inter,Re}} + i\sigma_{\text{inter,Im}}$ are the contributions from intraband and interband mechanisms to the overall surface conductivity, respectively, $I = |\mathbf{E}_\parallel|^2/2\eta_0$ is the optical intensity, $I_{\text{sat}} = E_{\text{sat}}^2/2\eta_0$ is the saturation intensity, and $\eta_0 = 120\pi\,\Omega$ is the impedance of free space.

In our work, we consider graphene layers which are characterized by a low value of the Fermi level. This parameter can be tuned via chemical doping or external electrostatic biasing and typically ranges from zero for pristine and unbiased graphene to approximately 1 eV. In the optical regime and under the condition $|\mu_c| < \hbar\omega/2$, the interband term becomes dominant, allowing us to use the model of Eq. (1) while multiphoton processes, such as TPA or related phenomena, can be neglected as being much weaker [20].

B. Perturbation theory and SA

Perturbation theory is employed to determine the complex frequency shift $\Delta\omega$ induced by the saturable surface conductivity of graphene in a resonant structure. It is expected that $\Delta\omega$ is purely imaginary, since loss saturation, appearing in a nonwaveguiding sheet, is not supposed to alter the resonance frequency. We first define the unperturbed and perturbed fields through Maxwell's curl equations in the frequency domain (spatial dependence is suppressed),

$$\nabla \times \mathbf{E}_0 = -i\omega_0\mu_0\mathbf{H}_0, \tag{2a}$$

$$\nabla \times \mathbf{H}_0 = i\omega_0\varepsilon_0\varepsilon_r\mathbf{E}_0 + i\sigma_{\text{Im}}\delta_s(\mathbf{r})\mathbf{E}_{0,\parallel}, \tag{2b}$$

$$\nabla \times \mathbf{E} = -i\omega\mu_0\mathbf{H}, \tag{2c}$$

$$\nabla \times \mathbf{H} = i\omega\varepsilon_0\varepsilon_r\mathbf{E} + i\sigma_{\mathrm{Im}}\delta_s(\mathbf{r})\mathbf{E}_\parallel + \frac{\sigma_{\mathrm{inter,Re}}}{1+I/I_{\mathrm{sat}}}\delta_s(\mathbf{r})\mathbf{E}_\parallel, \tag{2d}$$

where $\sigma_{\mathrm{Im}} = \sigma_{\mathrm{intra,Im}} + \sigma_{\mathrm{inter,Im}}$ is the imaginary part of the total surface conductivity of graphene, $\delta_s(\mathbf{r})$ is the surface Dirac function, and $\exp\{+i\omega t\}$ is used as the harmonic-time convention. The imaginary part of the surface conductivity is included in the linear problem. Equivalently, this term could have been treated perturbatively, resulting in a constant resonance frequency shift, which is easily calculated through the linear problem. Both approaches lead to identical results. Note also that we have completely disregarded the real part of the intraband conductivity, as it is negligible compared to the interband counterpart for $|\mu_c| < \hbar\omega/2$. Total losses are dominated by the resistive losses of graphene and, thus, bulk materials are considered as lossless (the electric permittivity ε_r is real). In addition, the dispersion of linear properties (in particular, electric permittivity of silicon and surface conductivity of graphene) is sufficiently mild in the near infrared and thus will not enter in our calculations [13].

Using the conjugated form of the reciprocal theorem [38,39], accurate for lossless and nearly lossless systems, we construct the function $\mathbf{F} = \mathbf{E}_0^* \times \mathbf{H} + \mathbf{E} \times \mathbf{H}_0^*$ and calculate its divergence:

$$\nabla \cdot \mathbf{F} = -\,i(\omega-\omega_0)\mu_0\mathbf{H}\cdot\mathbf{H}_0^* - i(\omega-\omega_0)\varepsilon_r\varepsilon_0\mathbf{E}\cdot\mathbf{E}_0^* - \frac{\sigma_{\mathrm{inter,Re}}}{1+|\mathbf{E}_\parallel|^2/E_{\mathrm{sat}}^2}\delta_s(\mathbf{r})\mathbf{E}_\parallel\cdot\mathbf{E}_{0,\parallel}^*. \tag{3}$$

Following, the Gauss' divergence theorem is applied in a sufficiently expanded d-dimensional domain Ω ($d = \{2,3\}$ for two- and three-dimensional geometries, respectively), which is enclosed by a $(d-1)$-dimensional boundary Γ. Under fairly low radiation losses, it is acceptable to consider that $\int_\Omega \nabla\cdot\mathbf{F}\ d^dr = \oint_\Gamma \mathbf{F}\cdot\mathbf{n}\ d^{(d-1)}r = 0$ [12], where $\mathbf{n}$ is the normal outward vector to the boundary Γ. Then, we can write Eq. (3) as

$$0 = -\,i\Delta\omega\int\mu_0\mathbf{H}\cdot\mathbf{H}_0^*\ d^dr - i\Delta\omega\int\varepsilon_0\varepsilon_r\mathbf{E}\cdot\mathbf{E}_0^*\ d^dr - \int\frac{\sigma_{\mathrm{inter,Re}}}{1+|\mathbf{E}_\parallel|^2/E_{\mathrm{sat}}^2}\mathbf{E}_\parallel\cdot\mathbf{E}_{0,\parallel}^*\ d^{d-1}r, \tag{4}$$

where $\Delta\omega = \omega - \omega_0$ is the resonance frequency shift due to the saturable losses of the graphene sheet. We apply first-order perturbation theory by assuming that graphene resistive losses do not alter significantly the resonance mode, i.e., $\mathbf{E} \approx \mathbf{E}_0$, $\mathbf{H} \approx \mathbf{H}_0$. Solving Eq. (4) for $\Delta\omega$, we obtain

$$\frac{1}{\tau_{\mathrm{SA}}} = \mathrm{Im}\{\Delta\omega\} = \frac{\displaystyle\int\frac{\sigma_{\mathrm{inter,Re}}}{1+|\mathbf{E}_{0,\parallel}|^2/E_{\mathrm{sat}}^2}|\mathbf{E}_{0,\parallel}|^2\ d^{d-1}r}{\displaystyle\int(\mu_0|\mathbf{H}_0|^2+\varepsilon_0\varepsilon_r|\mathbf{E}_0|^2)\ d^dr}, \tag{5}$$

where τ_{SA} denotes the cavity photon lifetime corresponding to resistive losses of graphene under the effect of saturable absorption. As anticipated, the frequency shift $\Delta\omega$ is purely imaginary resulting in a single loss term τ_{SA}. The integration in the numerator of Eq. (5) is reduced by one order because of the sheet nature of graphene. Note also that the denominator can be identified as the quadruple of the total stored energy $W = (1/4)\int(\mu_0|\mathbf{H}_0|^2 + \varepsilon_0\varepsilon_r|\mathbf{E}_0|^2)\ d^dr$ in the resonator.

C. Coupled-mode theory and SA

The theoretical framework is completed by incorporating the saturable absorption effect into the temporal coupled-mode theory to analyze the response of nonlinear resonant structures. According to CMT, a system consisting of a traveling-wave resonator, side coupled to a straight waveguide, is described by the pair of equations [40,41]

$$\frac{da}{dt} = i\omega_0 a - \left(\frac{1}{\tau_{\mathrm{SA}}} + \frac{1}{\tau_{\mathrm{rad}}} + \frac{1}{\tau_e}\right)a + i\sqrt{\frac{2}{\tau_e}}s_i, \tag{6a}$$

$$s_t = s_i + i\sqrt{\frac{2}{\tau_e}}a, \tag{6b}$$

where τ_{rad} and τ_e are the photon cavity lifetimes corresponding to the radiative and coupling (external) losses, respectively. We have deliberately included only the radiative part of the total intrinsic losses in the resonator, as resistive losses are introduced to Eq. (6a) through the power-dependent parameter τ_{SA}. Although trivial under the examined conditions, losses from the intraband term can be easily integrated to any power-independent loss term; choosing the radiative term gives the effective parameter $(\tau_{\mathrm{rad}}^{\mathrm{eff}})^{-1} = \tau_{\mathrm{rad}}^{-1} + \tau_{\mathrm{intra}}^{-1}$, where τ_{intra} denotes the fixed photon cavity lifetime due to intraband absorption. The amplitude of the field in the cavity a is normalized so that $|a|^2 \equiv W$ expresses the total stored energy in the cavity. Similarly, s_i, s_t denote the amplitude of the incident and the transmitted wave, respectively, and are normalized so that $|s|^2$ expresses guided power.

Coupled-mode theory treats the resonator as a lumped element, while the calculation of the lifetime parameter τ_{SA} in Eq. (5) involves the spatially dependent values of the tangential electric-field components $\mathbf{E}_{0,\parallel}$. To overcome this complication, we first define the reference electric and magnetic fields, measured respectively in $\sqrt{\mathrm{V/(A\,m^2s)}}$ and $\sqrt{\mathrm{A/(V\,m^2s)}}$, as $\{\mathbf{E}_{\mathrm{ref}},\mathbf{H}_{\mathrm{ref}}\} = \{\mathbf{E}_0/\sqrt{W},\mathbf{H}_0/\sqrt{W}\}$, so that the total stored energy in the resonator equals one, i.e., $|a_{\mathrm{ref}}|^2 = 1$. Note that a_{ref} is a unitless parameter. Total stored energy is proportional to the square of electric- and magnetic-field values in every position [42]. Hence we can calculate the photon lifetime τ_{SA} with respect to $|a|^2$ by substituting the field distribution $\{|a|\mathbf{E}_{\mathrm{ref}},|a|\mathbf{H}_{\mathrm{ref}}\}$ to Eq. (5), i.e.,

$$\frac{1}{\tau_{\mathrm{SA}}} = \frac{1}{4}\int\frac{\sigma_{\mathrm{inter,Re}}}{1+|a|^2|\mathbf{E}_{\mathrm{ref},\parallel}|^2/E_{\mathrm{sat}}^2}|\mathbf{E}_{\mathrm{ref},\parallel}|^2\ d^{d-1}r, \tag{7}$$

where $\mathbf{E}_{\mathrm{ref},\parallel}$ are the tangential to the graphene sheet components of $\mathbf{E}_{\mathrm{ref}}$ and we have used the fact that $|a_{\mathrm{ref}}|^2 = (1/4)\int(\mu_0|\mathbf{H}_{\mathrm{ref}}|^2 + \varepsilon_0\varepsilon_r|\mathbf{E}_{\mathrm{ref}}|^2)\ d^dr = 1$. To numerically solve the CMT equations defined in Eqs. (6), we first calculate the reference fields through an unperturbed electromagnetic problem and, then, for each temporal step and corresponding stored energy $|a|^2$ we compute the photon lifetime τ_{SA} through Eq. (7).

In the special case of uniform electric-field values $|\mathbf{E}_{0,\parallel}|$ along the graphene sheet (anticipated in traveling-wave resonators with unidirectional excitation, where no standing pattern is formed), we can obtain a simple linear expression between photon lifetime τ_{SA} and stored energy in the resonator $|a|^2$

$$\tau_{\mathrm{SA}} = \tau_{\mathrm{SA},0}\left(1 + \frac{|a|^2}{W_{\mathrm{sat}}}\right), \tag{8}$$

where $\tau_{\mathrm{SA},0}$ denotes the cavity photon lifetime due to resistive losses in the limit of vanishingly small electric-field intensities and $W_{\mathrm{sat}} = (E_{\mathrm{sat}}/|\mathbf{E}_{\mathrm{ref},\parallel}|)^2$ is the equivalent saturation energy (the value of the total stored energy for which the relaxation time τ_{SA} doubles). The linear model of Eq. (8) is adequately precise in resonators with a high level of symmetry, which imposes electric-field values of the same order along the graphene layer.

To better understand the impact of SA in a resonant scheme, we first examine its continuous-wave (cw) response. For simplicity, we take into account only the saturable absorption through the simplified model of Eq. (8). This approach leads to accurate results when SA is the dominant phenomenon and, more importantly, it allows us to derive a single polynomial expression for describing the nonlinear response of the system. By assuming a constant field amplitude in the cavity $a(t) = \tilde{a}\exp\{i\omega t\}$, we conclude from Eqs. (6a) and (6b) that

$$T \equiv \frac{P_{\mathrm{out}}}{P_{\mathrm{in}}} = \frac{\delta^2 + \left(\frac{1}{1+|\tilde{a}|^2/W_{\mathrm{sat}}} - r_e\right)^2}{\delta^2 + \left(\frac{1}{1+|\tilde{a}|^2/W_{\mathrm{sat}}} + r_e\right)^2}, \tag{9}$$

where T is the power transmission coefficient, $P_{\mathrm{in}} = |s_i|^2$ and $P_{\mathrm{out}} = |s_t|^2$ are the input and output power in the bus waveguide, $\delta = \tau_{\mathrm{SA},0}(\omega - \omega_0)$ is the normalized detuning parameter, and $r_e = \tau_{\mathrm{SA},0}/\tau_e$. In the derivation of Eq. (9) we have neglected radiation losses, as in many cases (including the example considered in Sec. III) they are much lower than resistive or coupling losses; yet they can be easily incorporated as an extra, similar to r_e, term. Under this condition, it holds that $\tau_{\mathrm{SA}} \approx 2Q_i/\omega_0$ (Q_i is the power-dependent intrinsic quality factor) and we can write

$$|\tilde{a}|^2 = Q_i\frac{P_{\mathrm{in}} - P_{\mathrm{out}}}{\omega_0} = \frac{\tau_{\mathrm{SA},0}}{2}\left(1 + \frac{|\tilde{a}|^2}{W_{\mathrm{sat}}}\right)(P_{\mathrm{in}} - P_{\mathrm{out}}), \tag{10}$$

where we have used the simple model of Eq. (8) for the photon lifetime τ_{SA}. Solving Eq. (10) for $|\tilde{a}|^2$ and making use of Eq. (9), we finally arrive at

$$\frac{p_{\mathrm{out}}}{p_{\mathrm{in}}} = \frac{\delta^2 + (1 - p_{\mathrm{in}} + p_{\mathrm{out}} - r_e)^2}{\delta^2 + (1 - p_{\mathrm{in}} + p_{\mathrm{out}} + r_e)^2}, \tag{11}$$

where we have introduced the normalized power levels as $p_{\mathrm{in}} = P_{\mathrm{in}}/P_0^{\mathrm{SA}}$ and $p_{\mathrm{out}} = P_{\mathrm{out}}/P_0^{\mathrm{SA}}$. The parameter

$$P_0^{\mathrm{SA}} = \frac{2W_{\mathrm{sat}}}{\tau_{\mathrm{SA},0}} \tag{12}$$

stands for the characteristic power of saturable absorption and it is associated with the power level at which the SA-related phenomena become important.

Equation (11) is a simple third-order polynomial expression allowing one to calculate the transmission of the system. Its normalized form makes it independent of the underlying system, yet it can be concretized providing the appropriate parameter set $\{P_0^{\mathrm{SA}}, \delta, r_e\}$. Initially, we use Eq. (11) in order to investigate the effect of the ratio r_e on the power transmission curve. In Fig. 1(a), we depict T as a function of the normalized input power for $\delta = 0$ and different values of r_e. As expected, for $r_e = 1$ we are under critical coupling conditions ($Q_i = Q_e$, or $\tau_{\mathrm{SA}} = \tau_e$) at low input power and transmission equals zero. For higher input power, SA manifests by suppressing losses and increasing the photon lifetime τ_{SA}. Therefore, the resonant system deviates from critical coupling and transmission in the bus waveguide increases. The opposite behavior is observed for $r_e < 1$, where the transmission is nonzero for low input power due to undercoupling conditions and eventually decreases to zero for a sufficient input power level when resistive losses are suppressed and critical coupling is met. Similarly, in Fig. 1(b) we examine the effect of normalized detuning to power transmission by setting $r_e = 0.25$ and appointing different

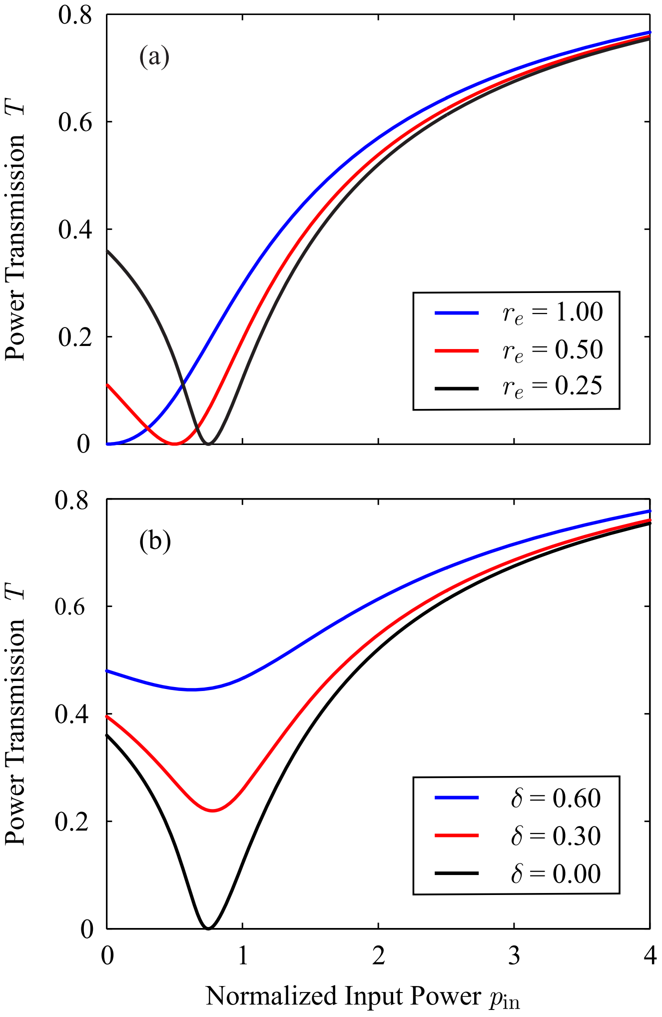

FIG. 1. Power transmission coefficient T versus normalized input power p_{in}. (a) $r_e = \{1,0.5,0.25\}$ for $\delta = 0$. Undercoupling ($r_e < 1$) shifts minimum transmission to higher p_{in}, while allowing for larger transmission under low input power. (b) $\delta = \{0,0.3,0.6\}$ for $r_e = 0.25$. When the operating frequency ω deviates from the resonance frequency ω_0 ($\delta \neq 0$), minimum transmission elevates, resulting in poor extinction.

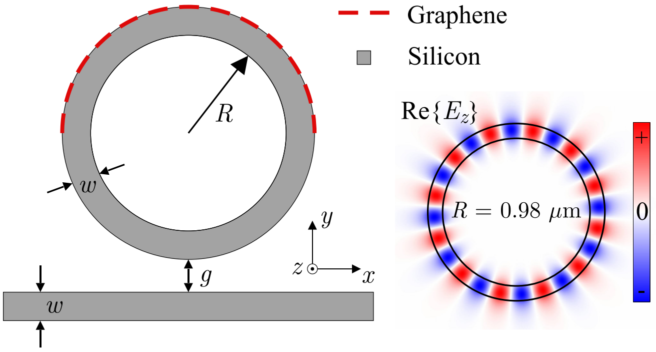

FIG. 2. Air-cladded nonlinear 2D ring resonator, side coupled to a bus waveguide through a coupling gap g. The resonance mode of the uncoupled resonator (shown in the inset) for a radius $R = 0.98\ \mu$m has an azimuthal order of $m = 12$ and a resonance wavelength of $\lambda_0 = 1550$ nm. The standing-wave pattern shown emerges from the superposition of two degenerate counterpropagating modes with equal amplitudes.

values to δ. Clearly, as δ increases, transmission increases as well. As we plan to exploit SA in the design of an all-optical switching element, it is essential to have the minimum power transmission at the low-output state in order to achieve a high extinction ratio (ER). Thus the case of $\delta = 0$ is ideal, since we can theoretically obtain $T = 0$ for an appropriate value of input power.

The so far developed CMT framework can be expanded in order to include other nonlinear effects of bulk and sheet materials. Details can be found in the Appendix. The generalized form of CMT equations will be the case of the example considered in Secs. III and IV.

III. GENERIC NONLINEAR SYSTEM FOR SA-INDUCED SWITCHING

Following the development of the nonlinear framework, in this section we analyze a generic 2D nonlinear ring resonator which is comprised of silicon and graphene, and is side coupled to a silicon bus waveguide. We first use this example to validate the theoretical framework described in Sec. II by comparing the results with full-wave nonlinear vectorial finite element method (VFEM) simulations. Moreover, we demonstrate the possibility of all-optical switching originating from saturable absorption in graphene layers.

A. Physical layout and properties

The physical system under consideration is depicted in Fig. 2. By studying a two-dimensional geometry, we are able to capture the qualitative behavior of the resonant system and to validate the developed framework without the need of highly priced 3D nonlinear simulations. The system consists of a silicon slab ring resonator of inner radius R and width w, which is side coupled to a straight silicon waveguide of the same width. Furthermore, we have employed a graphene sheet in the half of the outer perimeter of the ring resonator to introduce loss saturation to our design.

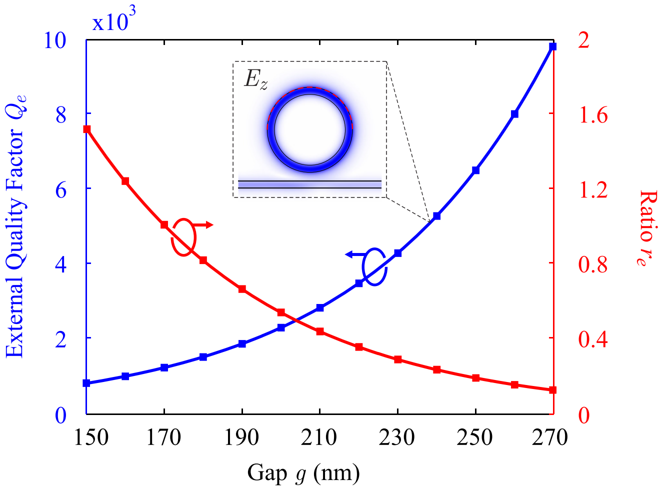

FIG. 3. External quality factor Q_e and ratio $r_e = \tau_{\mathrm{SA},0}/\tau_e$ versus the coupling gap g between the ring resonator and the bus waveguide. The selected condition $r_e = 0.25$ is satisfied for a coupling gap of 237 nm. Inset: E_z component of the electric field for $g = 237$ nm in the low-intensity limit, as obtained from a harmonic propagation simulation.

We focus our attention on the NIR which is widely used for communications and switching applications. At 1550 nm, we assign a constant linear refractive index $n_{\mathrm{Si}} = 3.478$ for Si [43]. Silicon also possesses nonlinear properties valued at $n_2^{\mathrm{Si}} = 2.5 \times 10^{-18}\ \mathrm{m}^2/\mathrm{W}$ and $\beta_{\mathrm{TPA}}^{\mathrm{Si}} = 5 \times 10^{-12}$ m/W, accounting for Kerr effect and TPA, respectively. As for graphene, working on a Fermi level of $\mu_c \approx 0$ results in linear surface conductivity terms $\sigma_{\mathrm{inter}} = 60.9\ \mu$S and $\sigma_{\mathrm{intra}} = 0.3 - i3.4\ \mu$S [36,37], with the interband contribution being dominant, as expected. We also assume a saturation intensity of $I_{\mathrm{sat}} = 1\ \mathrm{MW/cm}^2$, as values of this order have been demonstrated experimentally [27]. Lastly, graphene exhibits a nonlinear surface conductivity $\sigma_3 = -i1.2 \times 10^{-20}\ \mathrm{S(m/V)}^2$, which is derived by the measured equivalent nonlinear parameters $n_2 \approx -10^{-13}\ \mathrm{m}^2/\mathrm{W}$ and $\beta_{\mathrm{TPA}} \approx 0.9 \times 10^{-7}$ m/W [15,16]. The transformation process of bulk-equivalent parameters to nonlinear conductivity is outlined in Refs. [13,44].

Regarding geometrical parameters, the width of the ring resonator and the waveguide is set to $w = 200$ nm. The radius R of the ring resonator is appropriately selected to obtain a mode with the desirable resonance wavelength λ_0 and low radiative losses. For a radius of $R = 0.98\ \mu$m, we calculate $\lambda_0 = 1550$ nm and a resonant mode of azimuthal order $m = 12$ (depicted in the inset of Fig. 2). The TE polarization allows SA to manifest, through the interaction of the tangential component of the electric field, E_z, and the graphene sheets. Radiation losses are extremely low leading to an exceptionally high quality factor $Q_{\mathrm{rad}} \approx 3 \times 10^7$. On the other hand, graphene resistive losses dominate the total intrinsic losses of the resonator; in the low-intensity limit (without the effect of SA) we calculate $Q_{\mathrm{res}} = \omega_0 \tau_{\mathrm{SA},0}/2 = 1249$.

The coupling gap g between the ring resonator and the bus waveguide determines the coupling losses and subsequently the external quality factor, Q_e, of the resonator. We depict Q_e and the ratio r_e with respect to the gap in Fig. 3. Note that the lifetime parameter $\tau_{\mathrm{SA},0} = 2.06$ ps is calculated from the uncoupled problem and remains constant regardless of the coupling gap. Clearly, the external quality factor Q_e increases with g, as the coupling between the resonator and the waveguide weakens. Based on the findings of Sec. II C, we opt for undercoupling conditions in the low intensities limit, and more specifically for the $r_e = 0.25$ case. According to Fig. 3, this value corresponds to a coupling gap of $g = 237$ nm and an external quality factor of $Q_e = 4996$.

In order to introduce into the CMT equations nonlinear effects in addition to SA, we first have to compute the corresponding nonlinear coefficients γ describing the strength of each nonlinear phenomenon. Details on the expressions used for the calculation of Kerr, TPA, and FCEs coefficients can be found in the Appendix. It is also noted that we use a weakly coupled harmonic propagation simulation to obtain the electromagnetic field distribution necessary for estimating the parameters of the various nonlinear effects (the alternative calculation using an eigenvalue problem requires a specific correction in the case of traveling wave resonators [12]). We find that the Kerr effect induced by graphene ($\gamma_{\mathrm{Kerr,s}} = -6.2 \times 10^{17}\ \mathrm{W^{-1}s^{-2}m}$) outweighs the Kerr effect originating from silicon ($\gamma_{\mathrm{Kerr,b}} = 5.6 \times 10^{16}\ \mathrm{W^{-1}s^{-2}m}$); the overall response is identical to a defocusing material ($n_2 < 0$). It is also important that SA exhibits a relatively low characteristic power $P_0^{\mathrm{SA}} = 856$ W/m, while the characteristic powers of the Kerr effect and the free-carrier dispersion are $P_0^{\mathrm{Kerr}} = 2/(\tau_i^2|\gamma_{\mathrm{Kerr}}|) = 8.4 \times 10^5$ W/m and $P_0^{\mathrm{FCD}} = 2/(\tau_i^3\gamma_{\mathrm{FCD}})^{1/2} = 5.9 \times 10^5$ W/m, respectively (where the cavity lifetime τ_i is substituted with the SA parameter $\tau_{\mathrm{SA},0}$). Given that the characteristic power is a metric revealing the input power for which the respective effect becomes important, SA is expected to be the only nontrivial nonlinear effect for input power levels as high as 10^4 W/m.

B. Numerical validation

Having specified the geometrical parameters of the resonant system, we validate the accuracy of the CMT framework described in Sec. II under cw conditions. In particular, we feed Eq. (6) with an input power profile of a linear ramp function up to a fixed value and calculate the transmission after the system has been stabilized. We consider both the rigorous calculation of the power-dependent parameter τ_{SA} through Eq. (7) and its linear approximation in Eq. (8). In addition, we perform full-wave nonlinear VFEM simulations (including SA) using COMSOL Multiphysics® to assess the results obtained using CMT. Additionally, we study the effect of the other nonlinear phenomena by solving the generalized Eqs. (A1)–(A4) appearing in the Appendix. In Fig. 4 we plot the system transmission for input powers up to 10^4 W/m using the methods described above. We have also included the transmission curve using the model $\sigma_{\mathrm{inter,Re}}/\sqrt{1 + 3I/I_{\mathrm{sat}}}$ for the saturable term of graphene surface conductivity with the same value for the saturation intensity I_{sat} [20]. Although we do not use this model in what follows, recent theoretical studies have shown that SA in graphene scales with $1/\sqrt{I}$ in the limit of large incident intensities I. Despite the different SA models available in the literature, it is emphatically pointed out that the presented theoretical framework can handle any model for SA in graphene only with minor changes in the final expressions presented in this work, extracted strictly by using the model of Eq. (1).

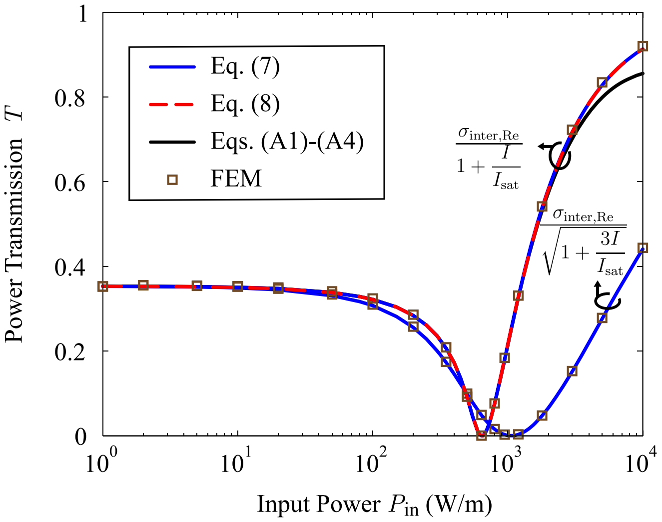

FIG. 4. Power transmission T under cw conditions for the resonant system of Fig. 2. CMT Eqs. (6) are solved, both with the exact expression of τ_{SA} through Eq. (7) (blue solid line) and the simple model of Eq. (8) (red dashed line). The calculated results are in perfect agreement with the nonlinear VFEM simulations (brown square markers). Kerr effect, TPA, and FCEs (black solid line) manifest only for higher input powers. The general trends are similar for the square-root model of SA, except for the smoother changes in transmission and the higher input power needed to reach critical coupling.

Figure 4 reveals excellent agreement between the transmission curves obtained through nonlinear simulations (brown markers) and CMT equations (blue solid line). The accuracy of the results is not affected when the simple approximation of Eq. (8) is applied to calculate the photon lifetime τ_{SA} (red dashed line). That is primarily due to the symmetry of the structure that imposes nearly constant values of the electric-field component E_z along the graphene sheet, as shown in the inset of Fig. 3. Note also that the inclusion of the Kerr effect, TPA, and FCEs modifies the transmission only for the larger input powers examined (black solid curve), as expected from the higher P_0^{Kerr} and P_0^{FCD} compared to P_0^{SA}.

For the saturation model of Eq. (1) transmission is 0.36 in the low intensities limit, drops to zero for $P_{\mathrm{in}} = 641$ W/m, and gradually increases to 1 for higher input powers. The overall behavior is similar, when the alternative square-root model is considered. Due to the weaker dependency of conductivity on electric field, the changes in transmission curve are smoother and a higher input power of 1061 W/m is necessary to reach critical coupling.

According to Ref. [45], SA in graphene may also modify the imaginary part of the interband conductivity term and induce a nonlinear resonance frequency shift. Following a procedure similar to that of Sec. II B, it is estimated that the SA-induced normalized frequency shift at the input power of 641 W/m is $\delta_{\mathrm{SA}} = -0.06$. The effect of this term regarding the cw transmission curve is negligible; the minimum transmission is 0.01% instead of zero. Nevertheless, the zero power transmission at the OFF state can be restored by applying a fixed detuning $\delta = +0.06$ to the frequency of input signal. In this case, the SA-induced frequency shift is fully counteracted for the input power of 641 W/m, while in the low intensity limit (where $\delta_{\mathrm{SA}} = 0$) the power transmission is slightly improved due to the nonzero detuning δ [cf. Fig. 1(b)].

C. Demonstration of all-optical switching

In order to design a functional all-optical switching element based on the resonant structure of Fig. 2, a control signal should be applied. In the absence of any control signal the low-power (1 W/m) probe signal is transmitted according to the cw transmission curve in Fig. 4 and the high-output (ON) state is achieved, though with moderate losses. To switch to the low-output (OFF) state, a control signal is applied, carrying an input power of $P_{\mathrm{in,c}}$, appropriately selected to render critical coupling of the probe signal, owing to the saturation of graphene losses.

However, the two signals propagate simultaneously in the same waveguide. Thus, to avoid distortion of the probe signal, they should be distinguishable in the frequency domain. Two options are considered for the central frequencies of probe and control signals. In the first, the two signals are placed in the same resonant mode with a sufficient detuning in the frequency of the control signal. For the second, the frequencies of the probe and control signals correspond to two consecutive resonances and thus the signals propagate in different resonant modes. Note that, in the first case, detuning should definitely refer to the control signal, since zero detuning of the probe signal is a prerequisite for attaining exactly zero transmission, as shown in Sec. II C. Inevitably, that will result in inferior coupling of the control signal and the power efficiency (in terms of necessary input power $P_{\mathrm{in,c}}$) will be reduced. Similarly, in the second case a portion of the input power $P_{\mathrm{in,c}}$ is not coupled to the resonator, as critical coupling conditions cannot be simultaneously met for both resonant modes due to the different cavity lifetime parameters.

To evaluate the performance of each option, we compute the transmission of the probe signal as a function of the control signal power. We solve a system of equations identical with those presented in Eqs. (6), encountering for two resonance modes, i.e., a_p and a_c for the probe and the control signal, respectively. The input power of the probe signal is set to $P_{\mathrm{in,p}} = 1$ W/m, which is insufficient for the saturation process to develop and thus SA is solely induced by the control signal. In Fig. 5, we depict transmission for a detuning of $\Delta\lambda = 0.2$ nm (the wavelengths of the probe and the control signal are $\lambda_p = 1550$ nm and $\lambda_c = 1549.8$ nm, respectively) and for two consecutive resonant modes ($\lambda_p = 1550$ nm and $\lambda_c = 1461$ nm, respectively). The corresponding normalized detuning for the control signal in the first scenario is $\delta_c = 0.32$. The cw curve of Fig. 4 is also included; although the two signals cannot be separated in this case, it serves as a lower bound for the required power $P_{\mathrm{in,c}}$ of the control signal. We observe that the selection of two consecutive resonances is advantageous in terms of the necessary power to switch to the OFF state. Specifically, an input power of $P_{\mathrm{in,c}} = 712$ W/m is required, which is lower than $P_{\mathrm{in,c}} = 876$ W/m needed even in the case of a small frequency detuning $\Delta\lambda = 0.2$ nm. That is because of the stronger coupling of the control signal to the resonator, when two resonant modes are considered, leading to better exploitation of the input power in the saturation of graphene losses. Note that a frequency detuning of $\Delta\lambda = 0.2$ nm (half of a typical channel bandwidth in a dense WDM system) is essential for the successful separation of two optical signals and higher detunings would result in even greater power demands. The results remain intact, even when considering saturation in the $\sigma_{\mathrm{inter,Im}}$, according to the model of Ref. [45].

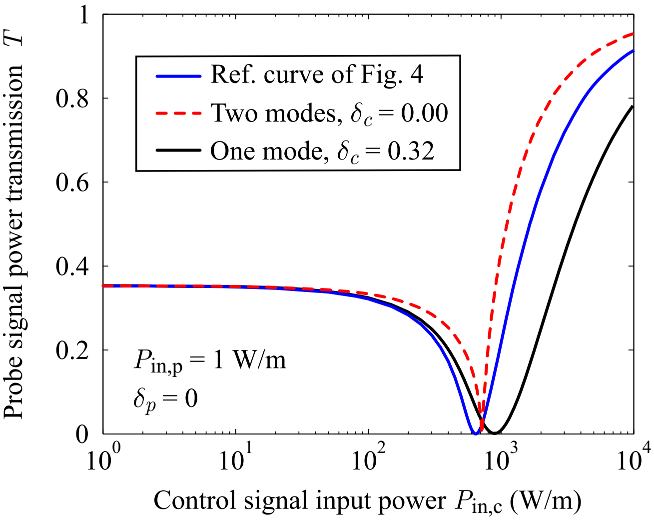

FIG. 5. Probe signal power transmission T under cw conditions versus the input power of the control signal $P_{\mathrm{in,c}}$. The option of two consecutive resonances for the distinction of the two signals (red dashed line) results in lower power requirements to reach the OFF state compared to the option of one resonant mode with a detuning of $\Delta\lambda = 0.2$ nm for the control signal (black solid line). The limiting and unrealistic case of identical frequencies is also depicted for comparison.

All-optical switching is demonstrated in Fig. 6, where the temporal response of the system is investigated using the CMT formalism developed. In particular, we assume that the probe signal consists of a train of super-Gaussian pulses with a full width at half maximum (FWHM) of 60 ps and a bit rate of 10 Gbps. The latter suggests that the bit duration is larger than the relaxation time of SA by at least two orders of magnitude, fully allowing one to model SA as an instantaneous phenomenon. The option of two successive resonances is used; probe and control signals have central wavelengths of 1550 nm and 1461 nm, respectively. The parameters characterizing the resonance mode used for the probe signal have been given in Sec. III A, while the resonant mode used for the control signal is characterized by $\tau_{\mathrm{SA},0} = 2.13$ ps, $Q_e = 10433$, and $r_e = 0.13$. For the numerical simulations of the resonant mode at $\lambda_c = 1461$ nm, the dispersion of silicon and graphene properties has been considered [36,43].

At first, the system operates at the high-output state and the probe signal is transmitted undistorted with maximum power of 0.36 W/m, in excellent agreement with the cw transmission in the low-intensity limit (Fig. 5). After the first three bits, a control signal of constant power $P_{\mathrm{in,c}} = 712$ W/m is applied in order to render critical coupling of the probe signal and shift operation to the low-output state. As observed,

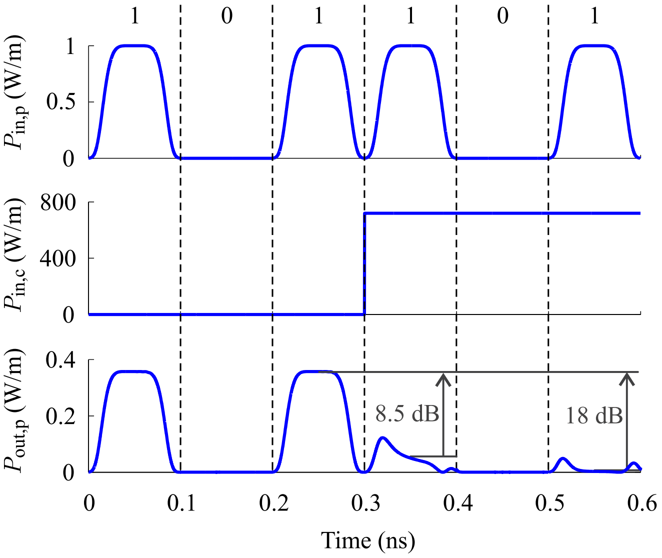

FIG. 6. Temporal response of the ring resonator system ($\lambda_p = 1550$ nm; $\lambda_c = 1461$ nm). All-optical switching is demonstrated with the control signal used to toggle the system to the OFF state. During the ON state (first three bits), the probe signal is transmitted undistorted, though with some attenuation, as predicted from the cw transmission curve of Fig. 5. When a control signal with $P_{\text{in,c}} = 712$ W/m is applied, the transmission is suppressed leading to an almost zero output with only limited transient effects appearing.

the transmission of the probe bitstream is greatly reduced and only limited transient phenomena exist, when a logical 1 is injected to the waveguide. Specifically, the higher transient effect appears just after the onset of the pumping. Assuming that the sampling is done in the center of each time slot, we find that the output powers of the fourth and the sixth bit are 8.5 dB and 18 dB lower than the transmission of logical 1 during the ON state. Note that we have considered the worst-case scenario in our demonstration, where both bits preceding and succeeding switching correspond to a logical 1. Every other case would result in an even weaker transient effect and a higher extinction between the two states. Lastly, it is pointed out that an appropriate detuning $\delta_p = \delta_c = -\delta_{\text{SA}}$ should be applied to counteract any SA-induced frequency shift, as discussed for cw conditions in Sec. III B.

Different design modifications can be applied in order to optimize the switching properties of the resonant system. First of all, the maximum transmission can be increased for smaller r_e, at the expense of higher power requirements to switch between states, as indicated in Fig. 1(a). Alternatively, the quality factor of the resonant system can be lowered, allowing it to respond faster and minimize the transient effects observed in Fig. 6. Finally, the pulse shape and duration can also be chosen appropriately to acquire the desired switching characteristics for the resonant system under study.

IV. NONLINEAR SYSTEM DYNAMICS

Although our analysis focused on the application of all-optical switching as demonstrated in Sec. III C, the nonlinear resonant system under investigation exhibits a rich dynamic behavior stemming from the interplay of different nonlinear phenomena in silicon and graphene. In particular, optical bistability (BI) and self-pulsation (SP) can be obtained for proper design selections and input power levels P_{in}. Through a linear stability analysis (details can be found in the Appendix) we distinguish between the regimes where BI, SP, or a combination of both can be observed.

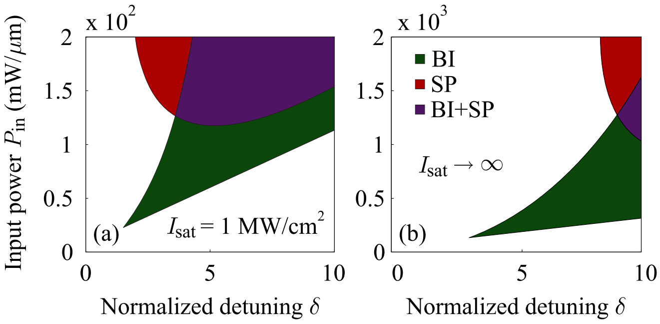

FIG. 7. BI and SP regions for $r_e = 1$ and $\tau_c/\tau_{\text{SA},0} = 0.97$. (a) SA is considered with $I_{\text{sat}} = 1$ MW/cm^2. (b) SA is neglected and graphene conductivity remains constant. A substantial growth in power requirements is observed for BI and SP owing to the absence of SA.

Self-pulsation can manifest when carrier and cavity lifetimes are of the same order of magnitude [35]. In our case, the cavity lifetime of the uncoupled ring is mainly determined by the power-dependent parameter τ_{SA}. On the other hand, the carrier lifetime is set to $\tau_c = 8$ ps. Typically in the order of ns, carriers lifetime can be reduced to the above-mentioned value through carrier sweeping, if a reverse biasing is applied by electrodes on the two sides of the ring resonator [46]. Alternatively, ion implantations can be introduced in Si, acting as traps for the free electrons, reducing τ_c [47]. To optimize bistability and self-pulsation in terms of the required input power, we appoint the value $\tau'_{\text{SA},0} = 4\tau_{\text{SA},0} = 8.24$ ps to the lifetime parameter in the low-intensity limit. Such a modification can easily be made by reducing the arc of the graphene sheet; due to the symmetry of the structure, a four times increase in $\tau_{\text{SA},0}$ is obtained by covering only a 45° arc of the outer ring perimeter (that will also result in a four times reduction in $\gamma_{\text{Kerr,s}}$ coefficient). Therefore, we get that $r_e = 1$ and $\tau_c/\tau_{\text{SA},0} = 0.97$. Both of these values are considered beneficial for the manifestation of self-pulsation, as will be demonstrated.

We predict the nature of the response for a range of detunings and input powers in order to specify the BI/SP regions in the δ-P_{in} plane. In Fig. 7(a), we illustrate the different regions, when considering SA in graphene. As observed, BI can be obtained for an input power as low as $P_{\text{in}} = 21$ mW/μm and a normalized detuning of $\delta \approx 1.4$. Because the Kerr effect in graphene overshadows the Kerr effect in Si, the Kerr-induced resonance frequency shift has the same sign as the FCD-induced frequency shift originating from Si. As a result, the two nonlinear phenomena act collaboratively for the appearance of bistability and the BI region spans only in positive detunings. Although a purely Kerr-induced BI appears exclusively for $\delta > 2\sqrt{3}$ [40], it is noted that FCEs and SA weaken significantly this requirement. SP also appears for an input power of $P_{\text{in}} \approx 127$ mW/μm both in combination with BI [purple (gray) region] and independently [red (light gray) region].

To analyze the effect of SA on the dynamics of the resonant system, we artificially assume that the graphene losses do not saturate ($I_{\mathrm{sat}} \rightarrow \infty$). The modified regions are specified through the same analysis and presented in Fig. 7(b). Obviously, the absence of SA shifts the BI/SP regions to higher input powers and detunings. Specifically, when SA is neglected, minimum power requirements are increased to 115 $\mathrm{mW}/\mu\mathrm{m}$ for BI and to 1.3×10^3 $\mathrm{mW}/\mu\mathrm{m}$ for a (pure) SP response. Therefore, we conclude that SA substantially facilitates the manifestation of optical bistability and self-pulsation at lower powers and smaller detunings. That is primarily due to the increase of the power-dependent cavity lifetime τ_{SA}, allowing for higher intrinsic quality factors.

V. CONCLUSION

To recapitulate, we have developed a rigorous framework for analyzing resonant structures exhibiting saturable absorption originating from graphene. The proposed framework is highly accurate, requires minimal computational resources, and gives a better physical insight of the loss saturation in resonant structures from the designer's point of view. Apart from the specific equation used to model graphene SA, we have shown that the framework can handle any model of closed-form equations characterizing SA, rendering it appropriate for describing instantaneous absorption saturation not only in graphene but in any other nonlinear bulk or sheet material with sufficiently complicated behavior. Furthermore, CMT allows the systematic incorporation of other nonlinear phenomena that appears in graphene and silicon, such as the Kerr effect, TPA, and FCEs, corroborating it as a dominant numerical tool set in the nonlinear resonator analysis and design process.

Based on the developed framework, we have demonstrated all-optical switching actions in a simple, yet representative example of a graphene-enhanced silicon slab ring resonator, side coupled to an access waveguide. Despite the fact that this work did not target on proposing a high-performance switch but hardly the framework capabilities, the resulting switching element presents satisfactory metrics (high ER, low operation power), which are promising for the design of practical all-optical switches in 3D, based on graphene saturable absorption. Besides, the resonant system evince rich dynamics (admitting bistability and self-pulsation), allowing for more elaborate actions that deem further study.

APPENDIX: GENERALIZATION OF CMT EQUATIONS, NORMALIZATION, AND STABILITY ANALYSIS

Following the introduction of saturable absorption into the CMT framework, we generalize Eq. (6a) to include the effect of several others nonlinear mechanisms. These are the Kerr effect of both sheet and bulk materials, two-photon absorption in silicon, and the emerged free-carrier dispersion and absorption. For a resonant structure that encompasses all the aforementioned nonlinear phenomena, the temporal evolution of the slowly varying envelope $\tilde{a}(t)$ is governed by the differential equation [34]

$$\begin{aligned}\frac{d\tilde{a}}{dt} &= i\big(\omega_0 - \omega - \gamma_{\mathrm{Kerr}}|\tilde{a}|^2 + \gamma_{\mathrm{FCD}}^{\mathrm{dyn}}\bar{N}\big)\tilde{a} \\ &\quad - \left(\frac{1}{\tau_{\mathrm{SA}}} + \frac{1}{\tau_{\mathrm{rad}}} + \frac{1}{\tau_e} + \gamma_{\mathrm{TPA}}|\tilde{a}|^2 + \gamma_{\mathrm{FCA}}^{\mathrm{dyn}}\bar{N}\right)\tilde{a} \\ &\quad + i\sqrt{\frac{2}{\tau_e}}\tilde{s}_i, \qquad \text{(A1)}\end{aligned}$$

where γ parameters describe the strength of the corresponding nonlinear mechanism. Equation (A1) strictly refers to traveling wave resonators, side coupled to a bus waveguide; for different resonant systems the last term in the right-hand side should be modified appropriately to describe the coupling conditions. The γ_{Kerr} and γ_{TPA} quantities include the contributions of both bulk and sheet materials, as defined in Ref. [13]. Specifically, for the Kerr effect originating from graphene and silicon the two contributing terms act in opposition and the sign of the total frequency shift depends on their relevant strength. We have also defined the FCEs parameters as

$$\gamma_{\mathrm{FCD}}^{\mathrm{dyn}} = \frac{1}{2}\omega_0\frac{\kappa_{\mathrm{FCE}}}{\kappa_N}\sigma_n, \qquad \text{(A2a)}$$

$$\gamma_{\mathrm{FCA}}^{\mathrm{dyn}} = \frac{1}{4}c_0\frac{\kappa_{\mathrm{FCE}}}{\kappa_N}\sigma_a, \qquad \text{(A2b)}$$

where κ_{FCE} and κ_N are dimensionless quantities defined in Ref. [34], $\sigma_n = 5.5 \times 10^{-27}$ m^3, and $\sigma_a = 14.5 \times 10^{-22}$ m^2 [48]. As Eq. (A1) indicates, γ parameters relate the stored energy $|\tilde{a}|^2$ or the carrier density $\bar{N}$ to a nonlinear resonance frequency shift or to nonlinear losses, depending on the nature of each nonlinear effect. They are all proportional to the respective nonlinear refractive index or nonlinear surface conductivity and to the corresponding dimensionless parameters κ measuring the overlap between the mode and the nonlinear materials. We also define $\bar{N}$ as a spatially averaged carrier density of the coordinate-dependent density N,

$$\bar{N} = \frac{\int N(\mathbf{r})|\mathbf{E}_0(\mathbf{r})|^2 d^d r}{\int |\mathbf{E}_0(\mathbf{r})|^2 d^d r}, \qquad \text{(A3)}$$

following the approach proposed in Ref. [49]. The temporal evolution of $\bar{N}$ is governed by

$$\frac{d\bar{N}}{dt} = -\frac{\bar{N}}{\tau_c} + \gamma_N|\tilde{a}|^4, \qquad \text{(A4)}$$

where τ_c is the free carrier lifetime and γ_N is a coefficient defined as in Ref. [34].

Equations (A1) and (A4) are difficult to handle numerically, as the involved variables differ by several orders of magnitude. To compensate for these differences, we employ a normalization procedure by defining the normalized quantities $\tilde{u} = \tilde{a}/W_{\mathrm{sat}}^{1/2}$, $\bar{n} = \bar{N}/(\tau_{\mathrm{SA},0}W_{\mathrm{sat}}^2\gamma_N)$, $\tilde{\psi} = \tilde{s}/(P_0^{\mathrm{SA}})^{1/2}$, and $t' = t/\tau_{\mathrm{SA},0}$ and reach

$$\begin{aligned}\frac{d\tilde{u}}{dt'} &= i\big(-\delta - r_{\mathrm{Kerr}}|\tilde{u}|^2 + r_{\mathrm{FCD}}^{\mathrm{dyn}}\bar{n}\big)\tilde{u} \\ &\quad - \left(\frac{1}{1+|\tilde{u}|^2} + r_{\mathrm{rad}} + r_e + r_{\mathrm{TPA}}|\tilde{u}|^2 + r_{\mathrm{FCA}}^{\mathrm{dyn}}\bar{n}\right)\tilde{u} \\ &\quad + i2\sqrt{r_e}\tilde{\psi}_i, \qquad \text{(A5a)}\end{aligned}$$

$$\frac{d\bar{n}}{dt'} = -\frac{\tau_{\mathrm{SA},0}}{\tau_c}\bar{n} + |\tilde{u}|^4, \qquad \text{(A5b)}$$

TABLE I. Dynamic behavior of Eq. (A1) solutions based on the eigenvalues of their respective $\boldsymbol{J}$ matrix.

cw solutions	1	3		
Stable	$\lambda^{\mathbb{R}} < 0$ $\mathrm{Re}\{\lambda^{\mathbb{C}}\} < 0$			
BI		$\lambda_1^{\mathbb{R}} < 0$ $\mathrm{Re}\{\lambda_1^{\mathbb{C}}\} < 0$	$\lambda_2^{\mathbb{R}} < 0$ $\mathrm{Re}\{\lambda_2^{\mathbb{C}}\} < 0$	$\lambda_3^{\mathbb{R}} > 0$ $\mathrm{Re}\{\lambda_3^{\mathbb{C}}\} < 0$
SP	$\lambda^{\mathbb{R}} < 0$ $\mathrm{Re}\{\lambda^{\mathbb{C}}\} > 0$			
BI + SP		$\lambda_1^{\mathbb{R}} < 0$ $\mathrm{Re}\{\lambda_1^{\mathbb{C}}\} > 0$	$\lambda_2^{\mathbb{R}} < 0$ $\mathrm{Re}\{\lambda_2^{\mathbb{C}}\} < 0$	$\lambda_3^{\mathbb{R}} > 0$ $\mathrm{Re}\{\lambda_3^{\mathbb{C}}\} < 0$

where we have introduced the ratios $r_e = \tau_{\mathrm{SA},0}/\tau_e$ and $r_{\mathrm{rad}} = \tau_{\mathrm{SA},0}/\tau_{\mathrm{rad}}$, the Kerr parameter $r_{\mathrm{Kerr}} = \gamma_{\mathrm{Kerr}}\tau_{\mathrm{SA},0}W_{\mathrm{sat}}$, the TPA parameter $r_{\mathrm{TPA}} = \gamma_{\mathrm{TPA}}\tau_{\mathrm{SA},0}W_{\mathrm{sat}}$, and the dynamic FCE parameters $r_{\mathrm{FCD}}^{\mathrm{dyn}} = \gamma_{\mathrm{FCD}}^{\mathrm{dyn}}\tau_{\mathrm{SA},0}^2W_{\mathrm{sat}}^2\gamma_N$ and $r_{\mathrm{FCA}}^{\mathrm{dyn}} = \gamma_{\mathrm{FCA}}^{\mathrm{dyn}}\tau_{\mathrm{SA},0}^2W_{\mathrm{sat}}^2\gamma_N$; all represent the relative strength of each nonlinear effect with respect to SA. The choice of a normalization based on SA is fully reasonable, as SA is the dominant nonlinear effect in the example presented in this work.

We also outline here a linear stability analysis allowing one to predict the manifestation of bistable or self-pulsing behavior in the optical response of the nonlinear system, since both the Kerr effect and free-carrier dispersion are present [35,50]. The analysis is based on the perturbation of the steady-state solutions of the normalized set of Eqs. (A5) [51,52]. We extend this analysis to allow for resonant systems that additionally exhibit SA. For each of the solutions $\{\tilde{u},\bar{n}\}$ in the steady state (three solutions exist in the case of bistability), we assume a small perturbation resulting in $\tilde{u}' = \tilde{u} + \delta\tilde{u}$ and $\bar{n}' = \bar{n} + \delta\bar{n}$. Neglecting second- or higher-order perturbative terms and using the approximation $1/(1+x) \approx 1 - x$ for $x \ll 1$, we write

$$\frac{1}{1+|\tilde{u}+\delta\tilde{u}|^2} \approx \frac{1}{1+|\tilde{u}|^2}\left(1 - \frac{\tilde{u}^*\delta\tilde{u} + \tilde{u}\delta\tilde{u}^*}{1+|\tilde{u}|^2}\right), \tag{A6}$$

and consider that the perturbation vector $\boldsymbol{\varepsilon} = [\delta\tilde{u}\ \ \delta\tilde{u}^*\ \ \delta\bar{n}]$, which satisfies the linear equation $d\boldsymbol{\varepsilon}/dt' = \boldsymbol{J}\boldsymbol{\varepsilon}$. The square matrix $\boldsymbol{J}$ has the form

$$\boldsymbol{J} = \begin{bmatrix} J_1 & J_2 & J_3 \\ J_2^* & J_1^* & J_3^* \\ J_4 & J_4^* & J_5 \end{bmatrix}, \tag{A7}$$

where the individual elements are given by

$$J_1 = i\left(-\delta - 2r_{\mathrm{Kerr}}|\tilde{u}|^2 + r_{\mathrm{FCD}}^{\mathrm{dyn}}\bar{n}\right) - \left(r_{\mathrm{rad}} + r_e + \frac{1}{1+|\tilde{u}|^2} - \frac{|\tilde{u}|^2}{(1+|\tilde{u}|^2)^2} + 2r_{\mathrm{TPA}}|\tilde{u}|^2 + r_{\mathrm{FCA}}^{\mathrm{dyn}}\bar{n}\right), \tag{A8a}$$

$$J_2 = -ir_{\mathrm{Kerr}}\tilde{u}^2 - r_{\mathrm{TPA}}\tilde{u}^2 + \frac{\tilde{u}^2}{(1+|\tilde{u}|^2)^2}, \tag{A8b}$$

$$J_3 = ir_{\mathrm{FCD}}^{\mathrm{dyn}}\tilde{u} - r_{\mathrm{FCA}}^{\mathrm{dyn}}\tilde{u}, \tag{A8c}$$

$$J_4 = 2|\tilde{u}|^2\tilde{u}^*, \tag{A8d}$$

$$J_5 = -\frac{\tau_{\mathrm{SA},0}}{\tau_c}. \tag{A8e}$$

The eigenvalues of $\boldsymbol{J}$ indicate whether bistability or self-pulsation appears for a given set of parameters in the $\delta - P_{\mathrm{in}}$ plane [35,51,52]. Specifically, $\boldsymbol{J}$ has a real eigenvalue $\lambda^{\mathbb{R}}$ and two complex conjugate eigenvalues $\lambda^{\mathbb{C}}$. A positive real eigenvalue corresponds to an unstable solution of Eq. (A1) (thus never practically observable), while a positive real part of the complex eigenvalues (Hopf bifurcation) corresponds to an oscillatory output, i.e., self-pulsation. All possible combinations of Eq. (A1) solutions with their respective eigenvalues and the expected dynamic behavior are gathered in Table I. In the most complex case, where bistability and self-pulsation are both present, it is noted that only the low-output state exhibits an oscillatory output, while the high-output state corresponds to a constant stable solution, as an insufficient number of free carriers develop in the resonator for the oscillation to take place.

[1] K. S. Novoselov, V. I. Fal'Ko, L. Colombo, P. R. Gellert, M. G. Schwab, and K. Kim, Nature (London) **490**, 192 (2012).

[2] P. Avouris, Nano Lett. **10**, 4285 (2010).

[3] F. Bonaccorso, Z. Sun, T. Hasan, and A. C. Ferrari, Nat. Photon. **4**, 611 (2010).

[4] M. Liu, X. Yin, E. Ulin-Avila, B. Geng, T. Zentgraf, L. Ju, F. Wang, and X. Zhang, Nature (London) **474**, 64 (2011).

[5] Q. Bao and K. P. Loh, ACS Nano **6**, 3677 (2012).

[6] A. Y. Nikitin, T. Low, and L. Martin-Moreno, Phys. Rev. B **90**, 041407 (2014).

[7] A. N. Grigorenko, M. Polini, and K. S. Novoselov, Nat. Photon. **6**, 749 (2012).

[8] S. A. Mikhailov, Europhys. Lett. **79**, 27002 (2007).

[9] J. L. Cheng, N. Vermeulen, and J. E. Sipe, New J. Phys. **16**, 053014 (2014).

[10] D. A. Smirnova, A. V. Gorbach, I. V. Iorsh, I. V. Shadrivov, and Y. S. Kivshar, Phys. Rev. B **88**, 045443 (2013).

[11] A. V. Gorbach and E. Ivanov, Phys. Rev. A **94**, 013811 (2016).

[12] T. Christopoulos, O. Tsilipakos, N. Grivas, and E. E. Kriezis, Phys. Rev. E **94**, 062219 (2016).

[13] T. Christopoulos, O. Tsilipakos, and E. E. Kriezis, J. Appl. Phys. **122**, 233101 (2017).

[14] E. Dremetsika, B. Dlubak, S.-P. Gorza, C. Ciret, M.-B. Martin, S. Hofmann, P. Seneor, D. Dolfi, S. Massar, P. Emplit, and P. Kockaert, Opt. Lett. **41**, 3281 (2016).

[15] N. Vermeulen, D. Castelló-Lurbe, J. Cheng, I. Pasternak, A. Krajewska, T. Ciuk, W. Strupinski, H. Thienpont, and J. Van Erps, Phys. Rev. Appl. **6**, 044006 (2016).

[16] G. Demetriou, H. T. Bookey, F. Biancalana, E. Abraham, Y. Wang, W. Ji, and A. K. Kar, Opt. Express **24**, 13033 (2016).

[17] T. Gu, N. Petrone, J. F. McMillan, A. Van Der Zande, M. Yu, G. Q. Lo, D. L. Kwong, J. Hone, and C. W. Wong, Nat. Photon. **6**, 554 (2012).

[18] M. Ji, H. Cai, L. Deng, Y. Huang, Q. Huang, J. Xia, Z. Li, J. Yu, and Y. Wang, Opt. Express **23**, 18679 (2015).

[19] Z. Zheng, C. Zhao, S. Lu, Y. Chen, Y. Li, H. Zhang, and S. Wen, Opt. Express **20**, 23201 (2012).

[20] A. Marini, J. D. Cox, and F. J. García de Abajo, Phys. Rev. B **95**, 125408 (2017).

[21] Q. Bao, H. Zhang, Y. Wang, Z. Ni, Y. Yan, Z. X. Shen, K. P. Loh, and D. Y. Tang, Adv. Funct. Mater. **19**, 3077 (2009).

[22] Z. Sun, T. Hasan, F. Torrisi, D. Popa, G. Privitera, F. Wang, F. Bonaccorso, D. M. Basko, and A. C. Ferrari, ACS Nano **4**, 803 (2010).

[23] W. B. Cho, J. W. Kim, H. W. Lee, S. Bae, B. H. Hong, S. Y. Choi, I. H. Baek, K. Kim, D.-I. Yeom, and F. Rotermund, Opt. Lett. **36**, 4089 (2011).

[24] D. Popa, Z. Sun, T. Hasan, F. Torrisi, F. Wang, and A. C. Ferrari, Appl. Phys. Lett. **98**, 073106 (2011).

[25] D. Li, H. Xue, M. Qi, Y. Wang, S. Aksimsek, N. Chekurov, W. Kim, C. Li, J. Riikonen, F. Ye, Q. Dai, Z. Ren, J. Bai, T. Hasan, H. Lipsanen, and Z. Sun, 2D Mater. **4**, 025095 (2017).

[26] A. A. Lagatsky, Z. Sun, T. S. Kulmala, R. S. Sundaram, S. Milana, F. Torrisi, O. L. Antipov, Y. Lee, J. H. Ahn, C. T. Brown, W. Sibbett, and A. C. Ferrari, Appl. Phys. Lett. **102**, 013113 (2013).

[27] Q. Bao, H. Zhang, Z. Ni, Y. Wang, L. Polavarapu, Z. Shen, Q.-H. Xu, D. Tang, and K. P. Loh, Nano Res. **4**, 297 (2011).

[28] C. A. Zaugg, Z. Sun, V. J. Wittwer, D. Popa, S. Milana, T. Kulmala, R. S. Sundaram, M. Mangold, O. D. Sieber, M. Golling, Y. Lee, J. H. Ahn, A. C. Ferrari, and U. Keller, Opt. Express **21**, 31548 (2013).

[29] K. Alexander, Y. Hu, M. Pantouvaki, S. Brems, I. Asselberghs, S.-P. Gorza, C. Huyghebaert, J. V. Campenhout, B. Kuyken, and D. V. Thourhout, *CLEO: 2015* (The Optical Society of America, San Jose, CA, 2015), p. STh4H.7.

[30] J. Wang, Z. Cheng, H. K. Tsang, and C. Shu, *OECC* (IEEE, Niigata, Japan, 2016), Vol. ThE3-2.

[31] M. Takahashi, W. Ueda, N. Goto, and S. Yanagiya, IEEE Photon. J. **5**, 6602109 (2013).

[32] H. A. Haus, *Waves and Fields in Optoelectronics* (Prentice-Hall, Englewood Cliffs, NJ, 1984).

[33] P. Ma, H. Jäckel, G. L. Bona, and C. Hafner, IEEE J. Quantum Electron. **50**, 1019 (2014).

[34] O. Tsilipakos, T. Christopoulos, and E. E. Kriezis, J. Lightw. Technol. **34**, 1333 (2016).

[35] S. Malaguti, G. Bellanca, A. de Rossi, S. Combrié, and S. Trillo, Phys. Rev. A **83**, 051802 (2011).

[36] D. Chatzidimitriou, A. Pitilakis, and E. E. Kriezis, J. Appl. Phys. **118**, 023105 (2015).

[37] G. W. Hanson, IEEE Trans. Antennas Propag. **56**, 747 (2008).

[38] A. W. Snyder and J. D. Love, *Optical Waveguide Theory* (Chapman and Hall, New York, 1983).

[39] S. V. Afshar and T. M. Monro, Opt. Express **17**, 2298 (2009).

[40] O. Tsilipakos and E. E. Kriezis, J. Opt. Soc. Am. B **31**, 1698 (2014).

[41] Q. Li, T. Wang, Y. Su, M. Yan, and M. Qiu, Opt. Express **18**, 8367 (2010).

[42] B. E. Little, S. T. Chu, H. A. Haus, J. Foresi, and J.-P. Laine, J. Lightw. Technol. **15**, 998 (1997).

[43] B. Tatian, Appl. Opt. **23**, 4477 (1984).

[44] R. del Coso and J. Solis, J. Opt. Soc. Am. B **21**, 640 (2004).

[45] A. Marini and F. J. García de Abajo, Phys. Rev. Lett. **116**, 217401 (2016).

[46] A. C. Turner-Foster, M. A. Foster, J. S. Levy, C. B. Poitras, R. Salem, A. L. Gaeta, and M. Lipson, Opt. Express **18**, 3582 (2010).

[47] M. Waldow, T. Plötzing, M. Gottheil, M. Först, J. Bolten, T. Wahlbrink, and H. Kurz, Opt. Express **16**, 7693 (2008).

[48] A. R. Motamedi, A. H. Nejadmalayeri, A. Khilo, F. X. Kärtner, and E. P. Ippen, Opt. Express **20**, 4085 (2012).

[49] G. Moille, S. Combrié, and A. De Rossi, Phys. Rev. A **94**, 023814 (2016).

[50] M. Soljačić, M. Ibanescu, S. G. Johnson, Y. Fink, and J. D. Joannopoulos, Phys. Rev. E **66**, 055601(R) (2002).

[51] S. Chen, L. Zhang, Y. Fei, and T. Cao, Opt. Express **20**, 7454 (2012).

[52] L. Zhang, Y. Fei, T. Cao, Y. Cao, Q. Xu, and S. Chen, Phys. Rev. A **87**, 053805 (2013).